J. Fluid Mech. (2014), *vol.* 756, *pp.* 328–353. © Cambridge University Press 2014
doi:10.1017/jfm.2014.382

Shock wave–boundary layer interactions in rectangular inlets: three-dimensional separation topology and critical points

W. Ethan Eagle[1],† and James F. Driscoll[1]

[1]Department of Aerospace Engineering, University of Michigan, Ann Arbor, MI 48109, USA

(Received 6 March 2014; revised 12 June 2014; accepted 26 June 2014;
first published online 2 September 2014)

The interaction between two separated flow regions was studied for the fundamental problem of a shock wave–boundary layer interaction (SBLI) within a rectangular inlet. One motivation is that the inlet of an engine on a supersonic aircraft may contain separation zones on the sidewalls and the bottom wall; if one region separates first it can alter the flow on the other wall and lead to engine unstart. In our work an oblique shock wave was generated by a wedge suspended from the upper wall of a Mach 2.75 wind tunnel. Stereo particle image velocimetry (PIV) measurements were recorded in 25 planes that include all three possible orthogonal orientations. The lateral velocity and vorticity measurements help to explain the underlying flow structure and these quantities were not measured previously for this problem. It is concluded that the sidewall and bottom wall separation zones interact due to an underlying flow structure that is similar to the two types of 3-D separation patterns previously described by Tobak & Peake (*Annu. Rev. Fluid Mech.*, vol. 14, 1982, pp. 61–85). Separation first occurs at an upstream location where the shock interacts with the sidewall. Lateral velocities direct flow toward the centreline to cause separation on the bottom wall. This causes significant curvature of the shock wave, so that even the region near the tunnel centreline cannot be explained by conventional 2-D concepts. A number of critical points (saddle points, nodes, focus points) were identified. Results are consistent with the general ideas of Burton & Babinsky (*J. Fluid Mech.*, vol. 707, 2012, pp. 287–306) and help to provide details of how the sidewalls redistribute the adverse pressure gradient in space.

Key words: boundary layer separation, high-speed flow

1. Introduction

1.1. *Statement of the problem*

The interaction between two separated flow regions is the focus of the present work; previously Bruce *et al.* (2011) and Burton & Babinsky (2012) have shown that reducing the size of one region can increase the size of the other. They explain that when an adverse pressure gradient is applied (by a complex 3-D shock wave structure, for example) the pressure gradient will be distributed in space. If suction is used to

† Email address for correspondence: eeagle@umich.edu

https://doi.org/10.1017/jfm.2014.382 Published online by Cambridge University Press

reduce the size of one separation region, a larger fraction of the total pressure gradient may be felt on the other region. They explain that compression waves generated by each region provide the mechanism for redistributing in space the pressure gradient. Délery (2001) and Helmer, Campo & Eaton (2012) also explain that an upstream separation region will divert the streamlines to create a lateral flow that can affect the other region. These previous studies point out the need to examine the underlying flow structure and to measure both the lateral velocities and the vorticity field.

One practical case of multi-wall separation occurs when an oblique shock wave within a rectangular duct causes separations on both the bottom and sidewall. This geometry is relevant because the inlet to an engine on a supersonic airplane may be approximately rectangular. When the non-separated core-flow area becomes too small the inlet will unstart (Hill & Peterson 1992). Therefore, it is useful to understand the locations and extent to which the area of the core flow is reduced by separation. Realistic engine inlets have small aspect ratios that may be less than one and there are no computational fluid dynamics (CFD) simulations that currently can adequately predict inlet unstart. This is partially due to the complexities associated with how the sidewall flow pattern affects the bottom wall region. No complete experimental database previously has existed that contains three velocity components and vorticity recorded on multiple perpendicular planes for a shock wave–boundary layer interaction (SBLI) within a rectangular duct.

To define the problem consider the oblique shock wave in the schematic that appears in figure 1. The shock wave is created by a full-span wedge that is suspended just below the top wall of a supersonic wind tunnel. The incident and reflected shock waves interact with the bottom wall and the sidewalls. This problem is of fundamental importance because it goes beyond previous 2-D SBLI problems and it represents a repeatable, well-defined 3-D flow separation problem that is governed primarily by four parameters:

$$(M_\infty, \theta, AR, Re_{\delta_o}). \tag{1.1}$$

Here M_∞ is the free-stream Mach number, θ is the deflection angle of the full-span wedge, AR is the duct aspect ratio (duct width divided by height) and Re_{δ_o} is the Reynolds number based on the boundary layer thickness (where $u/U_\infty = 0.95$) on the bottom wall at the wedge leading edge location. Values of these parameters for this study are: 2.75, 6.0°, 0.82 and 8.5×10^4; δ_o is 10.0 mm. Other minor parameters include the ratio of wall temperature to free-stream stagnation temperature (0.40) and the Prandtl number (0.72).

In figure 1 four regions of interest are marked A–D. The central region (A) lies on the bottom wall near the tunnel centreline. The present results show that it is not a simple 2-D separation bubble. A sidewall region (B) occurs where the incident shock bifurcates as it interacts with the sidewall. In region C the reflected shock also bifurcates near the sidewall. Region D is the corner where counter-rotating vortices exist. It will be shown that the incident shock wave becomes highly curved at its base. The curved dotted line on the bottom and sidewall is labelled the line of upstream influence. It it used to indicate how the first flow disturbances on the wall occur upstream of the shock position.

1.2. *Previous related SBLI research*

Interactions between separation zones within a rectangular duct previously have been investigated by Doerffer & Dallmann (1989), Dupont *et al.* (2005), Bruce *et al.* (2011), Burton, Babinsky & Bruce (2011), Burton & Babinsky (2012) and

https://doi.org/10.1017/jfm.2014.382 Published online by Cambridge University Press

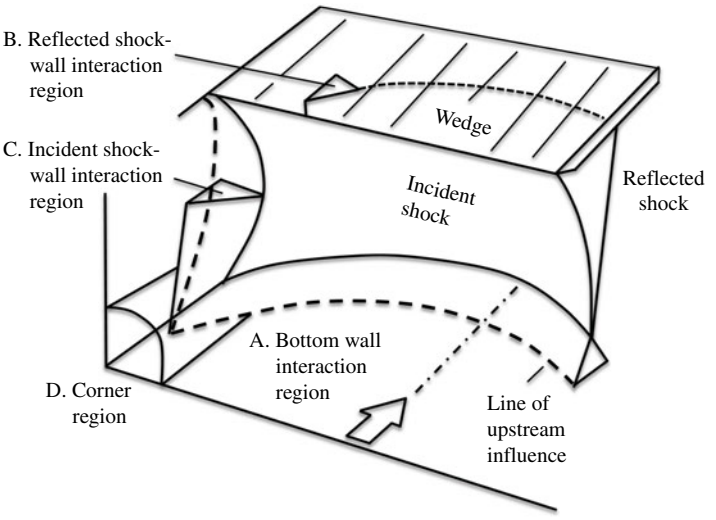


FIGURE 1. Schematic of an SBLI in a rectangular duct. Four regions of interest (A–D) are marked.

Helmer *et al.* (2012). The latter two papers report some velocity field measurements that were obtained with particle image velocimetry (PIV). The first three of these studies considered a normal shock wave at Mach numbers near 1.5 while the others considered the reflection of an oblique shock wave. A common conclusion of these papers is that they conjecture that the flow pattern is strongly affected by a lateral flow that is induced by sidewall separation, as well as by vortex structures. However, none of these studies report measurements of lateral velocities or the vorticity field. Doerffer & Dallmann (1989) stated that 'it is conjectured that streamwise-oriented vortices exist' based on saddle points and focus points in their wall oil film patterns. Burton & Babinsky (2012) also observed saddle points and focus points in oil film images. They reported a link between the size of the separated oil flow on the tunnel bottom wall and the size of their corner vortices. They concluded that this link is due to the generation of compression waves in the upstream corner. They discussed how waves emanating from the corner act to smear the adverse pressure gradient imposed upon other parts of the flow. Using the same wind tunnel, Bruce *et al.* (2011) varied several factors that affect the onset of separation and the sizes of separation regions. They found that modifying the corner region significantly affects the separation on the bottom wall, and they explain that altering the corner flow changed the shape of the shock wave. This modified the distribution of the pressure gradient in space. They reported that Mach number, tunnel aspect ratio and upstream boundary layer displacement thickness influenced their results.

Dupont *et al.* (2005) also concluded that the size of the bottom wall separation zone was affected by the flow on the tunnel sidewalls. For example, the bottom wall separation zone has an infinite extent in the lateral direction in the 2-D case, but this lateral extent became smaller as the aspect ratio of the duct was reduced. The effect of the sidewall also was discussed by Helmer *et al.* (2012). They used PIV to measure two velocity components but did not measure the lateral velocity or the vorticity because they did not use stereo-PIV. All four of their PIV data planes were parallel so orthogonal planes were not considered. It was concluded

https://doi.org/10.1017/jfm.2014.382 Published online by Cambridge University Press

that 'non-monotonic variations across the sidewall planes suggest the presence of significant spanwise flows' and 'It is proposed that corner vortices evolve into a single elongated vortical structure along the sidewall' but until now there has been no vorticity or lateral velocity data to assess this claim.

It is noted that the fin-sidewall problem is a separate SBLI problem that is not the topic of the present paper, but it provides useful insight. Panaras (1996) reviewed the work of Kubota & Stollery (1982) and Alvi & Settles (1992); analysis has been provided by van Oudheusden, Nebbeling & Bannink (1996). The fin is a wedge that is mounted on a sidewall. This problem differs from the rectangular duct problem because the field of interest does not include a bottom wall, a second confining sidewall or corner regions. Other sources of information are the reviews of the classic 2-D SBLI (Adamson & Messiter 1980; Délery & Dussauge 2009; Babinsky & Harvey 2011). For the case of a two-dimensional mean flow, extensive measurements and simulations were reported by Cantwell (1981), Dupont *et al.* (2005), Ganapathisubramani, Clemens & Dolling (2007), Humble, Scarano & van Oudheusden (2007), Dupont *et al.* (2008), Humble *et al.* (2009), Priebe, Wu & Martín (2009), Souverein *et al.* (2010) and DeBonis *et al.* (2012). Relevant mathematical analysis has been presented by Wu *et al.* (2000) and Surana, Grunberg & Haller (2006), Surana *et al.* (2008).

1.3. *Goals of this study*

The ultimate goal of this work is to determine the structure of the flow field associated with the interaction between the sidewall and the bottom wall separation regions for the case of an SBLI within a rectangular duct. The above studies point out the need for two additional pieces of information: lateral (horizontal) velocity data and vorticity measurements. The present work provides measurements of all 3 velocity components (using stereo-PIV) on 25 data planes that are aligned in 3 orthogonal directions.

Using this data, we evaluate previous ideas about the underlying flow structure. Using the general ideas of Tobak & Peake (1982) who theorized how lateral velocities could cause regions of upflow and downflow in 3-D geometries, we search our vorticity measurements to find evidence of horseshoe vortices. To fully quantify the flow structure, we look for critical points (these are defined below) in the velocity and oil film data. The final objective was to measure global features such as the curvature of the incident shock wave and the locations of upstream influence (where the flow is first disturbed). These features can be used in the future to assess CFD simulations. It is noted that the scope of the present paper is limited to flow topology; there is no discussion of our measurements of turbulence intensity, strain rates, Reynolds stresses or details of the wall pressure distribution; such a discussion is reserved for a future paper.

1.4. *Brief review of critical point theory*

To understand features native to three-dimensional flow separation, we will briefly review the concepts of topological critical points, and how to use oil flows to infer their existence. Then we examine the concepts of open versus closed separation and some sample topologies and vorticity patterns in 3-D separations are presented.

The present measurements are interrogated for evidence of critical points, so it is useful to first review canonical examples of Perry & Fairlie (1974), Tobak & Peake (1982), Perry & Chong (1987), Chong, Perry & Cantwell (1990) and Délery (2013). There are three types of critical points (nodes, saddle points and focus points) and figure 2 illustrates the skin friction lines that occur on the wall. A critical point on a

https://doi.org/10.1017/jfm.2014.382 Published online by Cambridge University Press

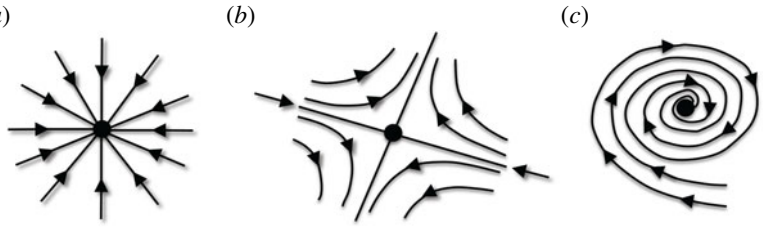


FIGURE 2. Limiting streamlines (skin friction lines) near the three types of critical points: (*a*) a separation node, (*b*) a saddle point and (*c*) a focus point, from Tobak & Peake (1982).

surface is defined to be a location where the magnitude of the two-dimensional skin friction vector is zero (Perry & Chong 1987). Near a separation node or a focus point the flow is directed inward so it rapidly lifts off the surface. At a saddle point the fluid on both sides is directed toward a separation line where it rapidly rises from the surface.

Limiting streamlines are defined to be the projection of the 3-D streamlines onto a plane that lies just above the wall. In steady, laminar, incompressible flows, it has been shown that limiting streamlines are identical to skin friction lines and oil streak lines (van Oudheusden *et al.* 1996). Squire (1961) has demonstrated that oil film lines are accurate markers of the skin friction lines in steady flows. Surana *et al.* (2008) pointed out that applying these concepts to unsteady, compressible flows may lead to errors. However, for qualitative explanations they remain useful. To see this, consider a horizontal (x–y) plane that is a distance h above the wall; the streamlines are solutions to

$$\frac{\mathrm{d}x}{U} = \frac{\mathrm{d}y}{V} \tag{1.2}$$

where U and V are velocities in the x and y directions, respectively. Skin friction lines are defined to be lines that are tangent to the local skin friction vector. That is, they are proportional to $(\tau_x \boldsymbol{i} + \tau_y \boldsymbol{j})$ in the x–y plane. Thus skin friction lines are solutions to

$$\frac{\mathrm{d}x}{\tau_x} = \frac{\mathrm{d}y}{\tau_y}. \tag{1.3}$$

For a Newtownian fluid, τ_x and τ_y are $\mu \mathrm{d}U/\mathrm{d}z$ and $\mu \mathrm{d}V/\mathrm{d}z$. In the limit of very small h, U and V vary linearly, thus $\mathrm{d}U/\mathrm{d}z = U/h$ and $\mathrm{d}V/\mathrm{d}z = V/h$. Inserting these values into (1.3) leads to (1.2).

There also is a need to differentiate between open and closed separation, as was pointed out by Wang (1972, 1974) and Wu *et al.* (2000). A classical 2-D separation bubble is closed since fluid in the bubble is separated from the bulk flow by the separation streamline. In contrast, two simple types of 3-D open separation are shown in figure 3 (Tobak & Peake 1982). In both cases, fluid that leaves the wall does not recirculate along a closed streamline.

The flow pattern in figure 3(*a*) is called a Type 1 separation; it has a leading edge saddle point. It is also characterized by limiting streamlines that diverge upstream of the leading edge, and by a horseshoe vortex that rotates in such a way that creates the down flow that is shown. In contrast, the flow pattern in figure 3(*b*) is called a Type 2 separation and it has a leading edge node. It is characterized by streamlines

https://doi.org/10.1017/jfm.2014.382 Published online by Cambridge University Press

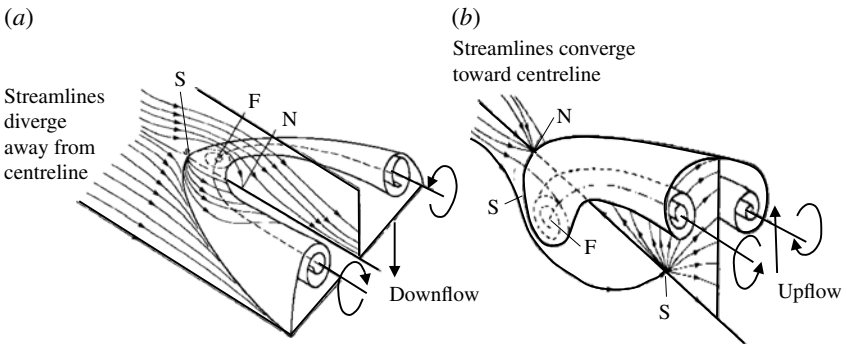


FIGURE 3. Two types of open 3-D separation described by Tobak & Peake (1982). (*a*) Type 1 separation has diverging streamlines at upstream locations and has downflow on centreline. (*b*) Type 2 separation has converging streamlines at upstream locations and has upflow on centreline.

that converge upstream of the leading edge, and by a horseshoe vortex that creates the upflow that is drawn.

For both cases the streamlines lift up away from the wall and they do not reattach. Some streamlines enter into the base of the vortex structures and then remain within these vortices, which extend far downstream. Other streamlines pass around the outside of the vortex structures but they always continue downstream. One way to create the flow seen in figure 3(*a*) is to mount a cylindrical post perpendicular to a wall. The post creates an adverse pressure gradient and a divergence in the upstream streamlines. Type 2 separation, however, requires convergence of limiting streamlines, which could be caused, for example, if there were two posts mounted perpendicular to the bottom wall and were located upstream and to the right and left of the pattern in figure 3(*b*).

The more complex 'owl-face' pattern in figure 4 is reproduced from Perry & Chong (1987) because it has features that are similar to the data described below. The owl-face has been observed when a cylindrical post is mounted perpendicular to a wall (Akilli & Rockwell 2002; Palau-Salvador *et al.* 2010), on the downstream side of a missile-shaped body at an angle of attack (Perry & Chong 1987) and on an aircraft wing (Kandasamy, Xing & Stern 2009). The leading edge of the owl-face in figure 4(*a*) is similar to the pattern in figure 3(*a*) in that it contains a saddle point (S) and the upstream streamlines diverge. In figure 4(*b*) a horseshoe vortex is parallel to the bottom wall and it intersects the vertical plane at the focus F. This horseshoe vortex rotates to create a downflow on the centreline, as does the vortex in figure 3(*a*). The downstream portion of the owl-face differs from figure 3(*a*) in that two focus points (F) and a reattachment node N occur on the bottom wall.

The owl-face is an open type of separation because there is no recirculating flow that is separate from the bulk flow. Fluid that approaches any of the focus points (F) will go inside the vortex structures and will be directed downstream. In the horizontal plane there is no closed streamline that starts at the centreline saddle point (S) and goes to the downstream attachment node (N), which is unlike the 2-D case. Délery (2001) suggest that the 2-D notion of 'reattachment' should be replaced with 'attachment' to signify that fluid attaching to the surface is not the fluid that had previously separated. Figure 4(*b*) also suggests that the horseshoe vortices play an important role in the creation of the distinctive owl-face flow pattern. Therefore, the present measurements were examined for the existence of horseshoe vortices.

https://doi.org/10.1017/jfm.2014.382 Published online by Cambridge University Press

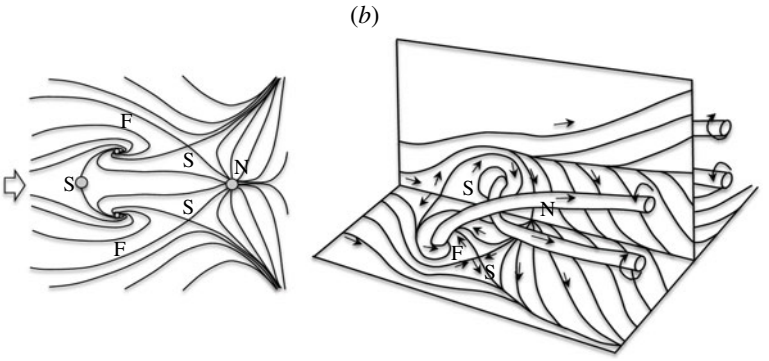


FIGURE 4. Owl-face pattern from Perry & Chong (1987). The leading edge is similar to Type 1 separation in figure 4(*a*) in that limiting streamlines diverge upstream of leading edge saddle point (S). Downstream there is a reattachment node (N). Also seen are other saddle (S) and focus points (F).

2. Experimental arrangement

2.1. *The supersonic wind tunnel and operating conditions*

A schematic of the Michigan supersonic wind tunnel appears in figure 5. The subsonic conditioning section is 254 mm high and 57.0 mm wide; it contains honeycomb and mesh screens. The nozzle throat is 18.5 mm high and 57.0 mm wide while the test section is 69.3 mm high and 57.0 mm wide. The unit Reynolds number is 8.5×10^6 m^{-1}. With our right-handed coordinate system the streamwise coordinate x is defined to be zero at the leading edge of the wedge. The throat is at $x = -475.5$ mm and the test section begins at $x = -331.5$ mm. The spanwise coordinate y is measured horizontally from the right sidewall as one looks downstream. The vertical coordinate z is measured vertically from the bottom wall. Optical access is provided by glass sidewalls along the entire length of the test section and by a glass panel located in the floor of the tunnel along the centreline. Additional details of the geometry are given in Eagle (2012) and Eagle, Driscoll & Benek (2012).

The oblique shock wave is generated by a six-degree full-span wedge that is suspended by a strut. The leading edge is 9.7 mm below the upper wall to place it outside of the upper wall boundary layer. With this design the shock wave remains attached to the wedge in a steady manner. If the wedge was mounted flush to the wall, then the upstream location of the shock would be unsteady. The upper surface of the wedge is angled downward at 2° with respect to the upper wall of the tunnel to provide expansion and prevent choking of the flow above the wedge.

The operating conditions are listed in table 1 and the maximum run time is 10 minutes. The quality of the flow in the test section and the uncertainties in the PIV data are discussed in appendix A. Previously, Lapsa & Dahm (2011) showed that boundary layer velocity profile at $x = -75.5$ mm agrees with Coles law of the wake down to a distance from the wall of 0.5 mm. Their measurements indicate that the boundary layer thickness (δ, where U is 95 % of its free-stream value) is 10.0 mm, the displacement thickness δ^* is 1.47 mm and the momentum thickness θ is 1.08. To compute these thicknesses, Lapsa & Dahm (2011) used a gas density profile that was measured in a previous study. The Reynolds numbers based on δ, δ^* and θ are 89 000, 13 100 and 9600, respectively.

https://doi.org/10.1017/jfm.2014.382 Published online by Cambridge University Press

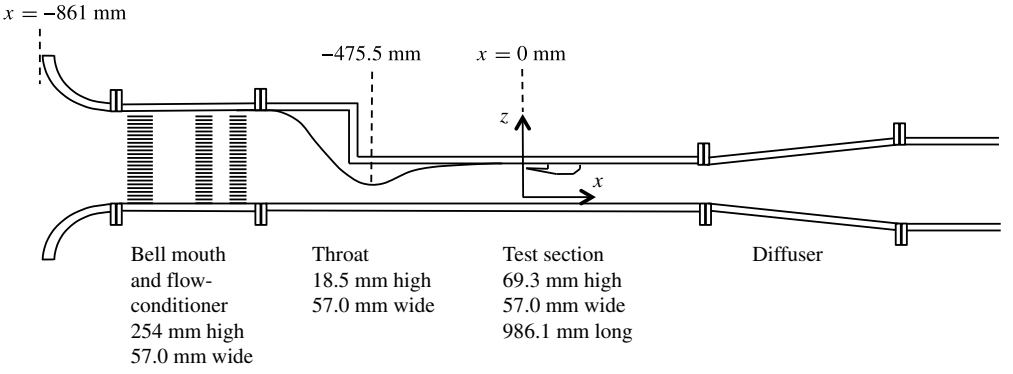


FIGURE 5. Schematic of the Michigan supersonic wind tunnel; x is the streamwise coordinate, y is the horizontal spanwise coordinate (into the paper) and z is the vertical coordinate.

Mach number M_∞	2.75	Stagnation temperature	295.7 K
Free-stream velocity U_∞	594 m s^{-1}	Stagnation pressure	98.6 kPa
Wedge leading edge	$x = 0$	Test section height	69.3 mm
Centre of shock reflection on centreline	$x = 96$ mm	Test section width	57.0 mm

TABLE 1. Mach 2.75 wind tunnel conditions.

2.2. *The stereo-PIV system and data planes*

The stereo-PIV system includes two Nd:YAG lasers, two SensiCam PCO interline transfer CCD cameras and two Sigma 70-300 f/4–5.6 macro lenses. Schiempflug optics were aligned at an angle of 33° to the light sheet. The energy of each 532 nm light sheet was 200 mJ per pulse. Three images per second were recorded on a 1024 pixel × 1280 pixel array that has a physical CCD chip size of 6.8 mm × 8.6 mm. The 12-bit signal depth provides sufficient signal dynamic range and electronic Peltier cooling ensures low noise. Air in the stagnation chamber was seeded with oil drops using a commercial monodisperse oil drop generator (TDA-4B, ATI Techniques, Inc.). The density of the poly-alpha olefin oil is 819 kg m^{-3}. The mean drop size was specified by the manufacturer to be 0.3 μm and was experimentally checked by Lapsa (2009). He measured the exponential decay of the particle velocity downstream of the oblique shock, where the gas velocity undergoes a step change. His measured decay time indicated that drop size was between 0.2 and 0.4 μm. He also showed that the oil drop velocity faithfully follows the air velocity to within 3 % except in the regions that are 1.9 mm (two interrogation window sizes) downstream of the incident and reflected shock waves. His findings are in agreement with particle tracking results of Clemens & Mungal (1991) and Samimy & Lele (1991).

The 25 PIV data planes are shown in figure 6 and their locations are listed in table 2. On each plane typically 1700 instantaneous PIV images were recorded and averaged to reduce statistical uncertainties as described in appendix A. The three streamwise vertical planes are denoted SV1, SV2 and SV3. The four streamwise horizontal planes that are denoted SH1 to SH4 are parallel to the bottom wall. The transverse vertical planes are TV1 to TV18. Data recorded on planes TV1 and TV2

https://doi.org/10.1017/jfm.2014.382 Published online by Cambridge University Press

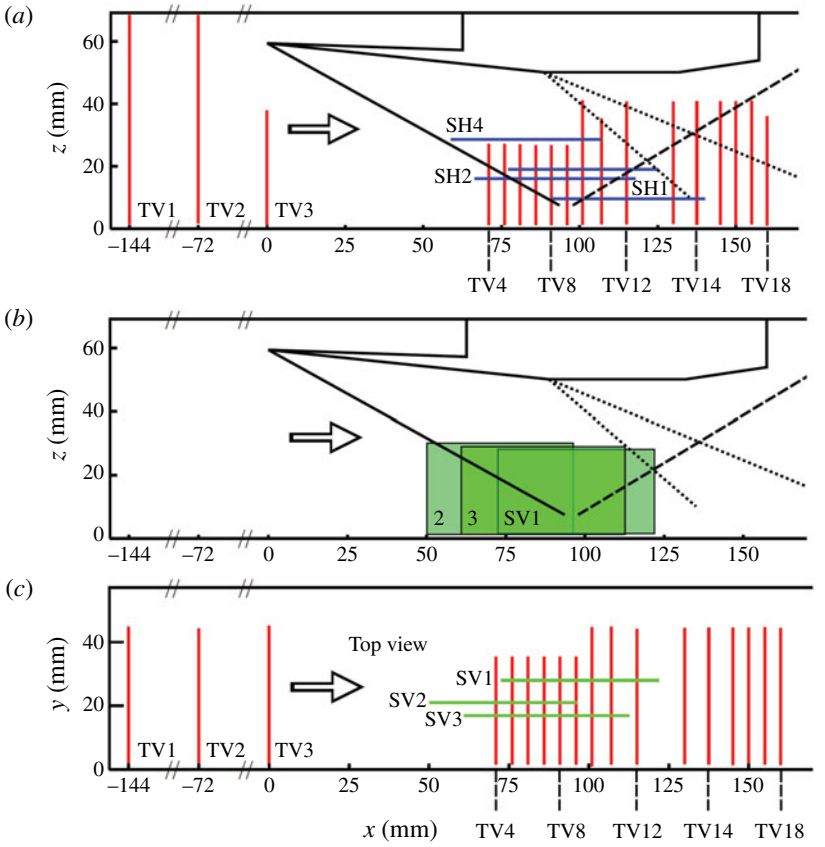


FIGURE 6. (Colour online) Schematic of the 25 PIV measurement planes and the coordinate system. Plane TV3 is located at $x = 0$, which is under the leading edge of the shock generator.

represent the upstream boundary conditions. Plane TV3 is at the wedge leading edge ($x = 0$ mm). Plane TV18 is where the outflow boundary conditions were measured.

Supersonic flow introduces several challenges that required a careful optimization of the time between laser pulses, the laser sheet thickness and the interrogation box size. Eagle *et al.* (2012) systematically varied these parameters and showed that the optimum values were 600 ns, 1.25 mm and 32 pixel × 32 pixel (0.49 mm × 0.49 mm). A challenge arises because it is desired to measure all three velocity components on each data plane. The streamwise velocity is nearly 600 m s^{-1} but lateral velocities as small as 20 m s^{-1} are of interest. Selecting 600 ns between the laser pulses allows two particle images to be collected during the transit time of a 600 m s^{-1} particle within a 1.25 mm thick laser sheet that is aligned transverse to the main flow. This time also was found to provide sufficient displacement of a 20 m s^{-1} particle that is moving parallel to the sheet.

3. Results

In § 3.1 we describe the mean 3-D velocity field (U, V and W) near the bottom wall region. The locations of critical points, the shapes of the curved incident and reflected shock waves and the size of the bottom wall interaction region are reported. In § 3.2

https://doi.org/10.1017/jfm.2014.382 Published online by Cambridge University Press

https://doi.org/10.1017/jfm.2014.382 Published online by Cambridge University Press

Plane	x (mm)	y (mm) Spanwise	z (mm) Vertical	
Transverse vertical planes				
TV1	−144	1.3–45	1.3–68	Upstream boundary condition
TV2	−72	1.8–44	1.6–68	Upstream boundary condition
TV3	0	1.2–45	1.2–38	Leading edge of wedge
TV4	71	1.5–35	1.1–27	
TV5	76	1.5–35	1.1–27	
TV6	81	1.5–35	1.1–27	
TV7	86	1.5–35	1.1–27	
TV8	91	1.5–35	1.1–27	
TV9	96	1.5–35	1.1–27	Centre of bottom Wall separation
TV10	101	1.1–45	1.2–41	
TV11	107	1.6–45	1.4–35	
TV12	115	1.6–44	1.4–41	
TV13	130	1.8–44	1.5–41	
TV14	137	1.5–45	1.2–41	
Transverse vertical planes, continued				
TV15	145	1.5–45	1.2–41	
TV16	150	1.5–45	1.2–41	
TV17	155	1.6–45	1.4–41	
TV18	160	1.4–44	1.2–37	Downstream boundary condition
Streamwise vertical planes				
SV1	72–122	28.5	1.6–28	Tunnel centreline
SV2	51–96	21	1.2–30	
SV3	61–113	17	1.2–30	Close to sidewall
Streamwise horizontal planes				
SH1	91–141	14–45	9.5	Close to bottom
SH2	65–120	14–44	16	
SH3	77–125	11–42	19	
SH4	59–107	1.5–30	29	

TABLE 2. The 25 PIV data planes locations and sizes. SV denotes streamwise vertical, SH is streamwise horizontal and TV is a transverse vertical plane; $x = 0$ is the leading edge of the shock generator and $x = 96$ mm is the centre of the shock reflection off the bottom wall.

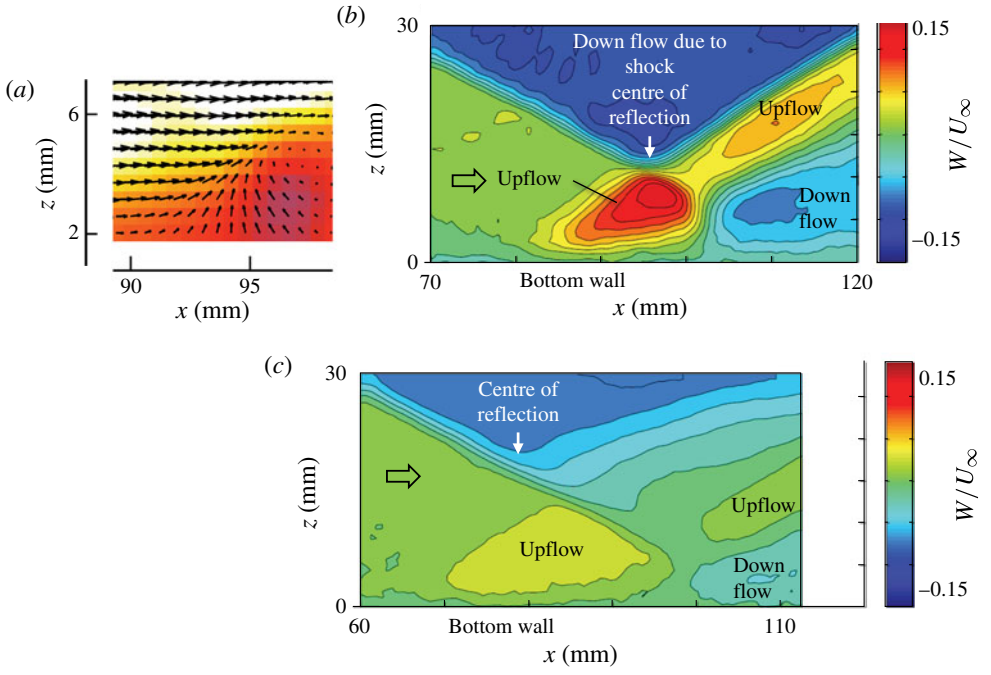


FIGURE 7. Bottom wall interaction region. (*a*) Instantaneous separation point determined from measured velocity vectors; (*b*) upflow and downflow deduced from contours of mean vertical velocity (W) at the tunnel centreline ($y = 28.5$ mm, plane SV1); and (*c*) between the sidewall and centreline ($y = 18$ mm, plane SV2). The centre of shock reflection is farther upstream at locations nearer the wall (*c*) than on the centreline (*b*).

we present evidence that Type 2 separation (figure 3*b*) occurs on the bottom wall near the centreline. In § 3.3 we describe the sidewall region and we present evidence that Type 1 separation (figure 3*a*) occurs on the sidewall.

3.1. *Bottom wall interaction region*

The features seen on the centreline plane SV1 in figure 7(*a*,*b*) are similar to that of a conventional 2-D oblique shock wave reflection. Contours of the mean vertical velocity (W) are plotted. At the top of figure 7(*b*) is a region of downflow that is caused by the turning of the flow by the incident shock. An arrow at $x = 96$ mm marks the centre of shock reflection. It is defined as the x-location where the downflow velocity region is closest to the bottom wall. Just below the centre of reflection is an oval-shaped upflow region followed by a downflow region. Behind the reflected shock at $x = 110$ mm is another upflow region. In the next section we argue that this upflow is due to the horseshoe vortex structure of a Type 2 separation. Figure 7(*a*) is a small portion of one instantaneous PIV image that shows that the velocity vectors near the instantaneous separation point look like a conventional saddle point in the x–z plane. This separation point moves in time over a distance of several millimetres and has an intermittent character.

Comparing figure 7(*b*) (centreline) and 7(*c*) (closer to the sidewall) shows that both the centre of reflection and the upflow region move upstream as you approach the sidewall. Contours of W are plotted in figure 7(*c*) for plane SV2 that is between the centreline and the sidewall. Note that the upflow velocity (W) near the centreline

https://doi.org/10.1017/jfm.2014.382 Published online by Cambridge University Press

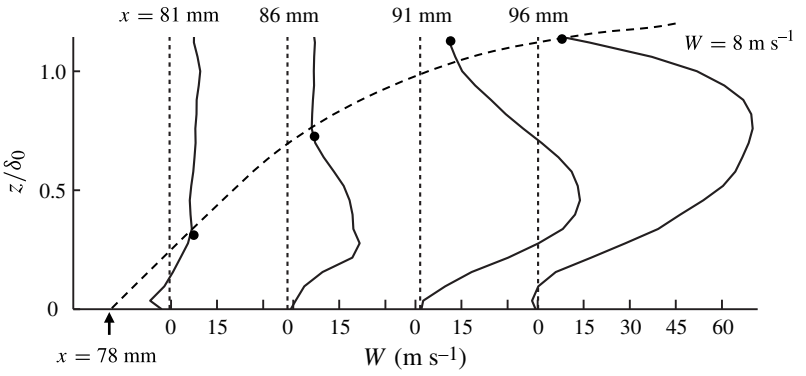


FIGURE 8. Side view of the bottom wall region, showing profiles of vertical velocity W versus vertical distance (z): (a) tunnel centreline ($y = 28.5$ mm, plane SV1); (b) closer to sidewall ($y = 17$ mm, plane SV3).

(figure 7*b*) is large but the maximum upward velocity becomes smaller and is more distributed as the sidewall is approached (figure 7*c*).

The vertical extent of the bottom wall interaction region is shown in figure 8. Profiles of the vertical mean velocity W are plotted versus the height off the wall, z. The dotted line indicates where $W = 8$ m s^{-1}. The dotted line intersects the bottom wall at $x = 78$ mm. The isoline $W = 8$ m s^{-1} was selected to visualize the extent of the disturbance to the core flow, but the reader may choose to select an isoline with a different value of W.

To better visualize the flow structure it was decided to employ the data analysis method of Adrian, Christensen & Liu (2000) and Adrian & Westerweel (2010). They define a 'Galilean decomposition streamline' in the x–z plane to be the solution to

$$\frac{\mathrm{d}x}{U - U_{AVG}} = \frac{\mathrm{d}z}{W - W_{AVG}} \tag{3.1}$$

where U and W are the mean velocities at each (x, z) location and (U_{AVG}, W_{AVG}) are velocities that are spatially averaged over the entire field of view for the 1700 instantaneous images. They have noted that any velocity field can be decomposed into a rotational component and an irrotational component. While the use of (3.1) does not exactly perform such a decomposition, it subtracts a convection velocity that makes vortical structures more visible.

Figure 9(*a*) indicates that spiral-shaped streamlines appear after (3.1) is applied to the PIV data for the centreline plane SV1. The spiral pattern indicates that below the shock reflection the velocity field has a large rotational component. The streamlines are seen to converge at the locations of the incident and reflected shocks. This is because the average convective velocity lies between the values of velocities that are upstream and downstream of each shock wave. For example, the vertical velocity is nearly zero upstream of the incident shock and downstream it is approximately -60 m s^{-1}. In the mean-convective frame of reference, the vertical velocity becomes $+30$ m s^{-1} upstream of the shock and is -30 m s^{-1} downstream.

To understand the transformation defined by (3.1), we also subtracted a larger convection velocity of (1.2 U_{AVG}, 1.2 V_{AVG}). The existence of critical points did not change, and the location of critical points did not move more than 2 mm. However, the streamline patterns around each critical point either expanded or compressed. It

https://doi.org/10.1017/jfm.2014.382 Published online by Cambridge University Press

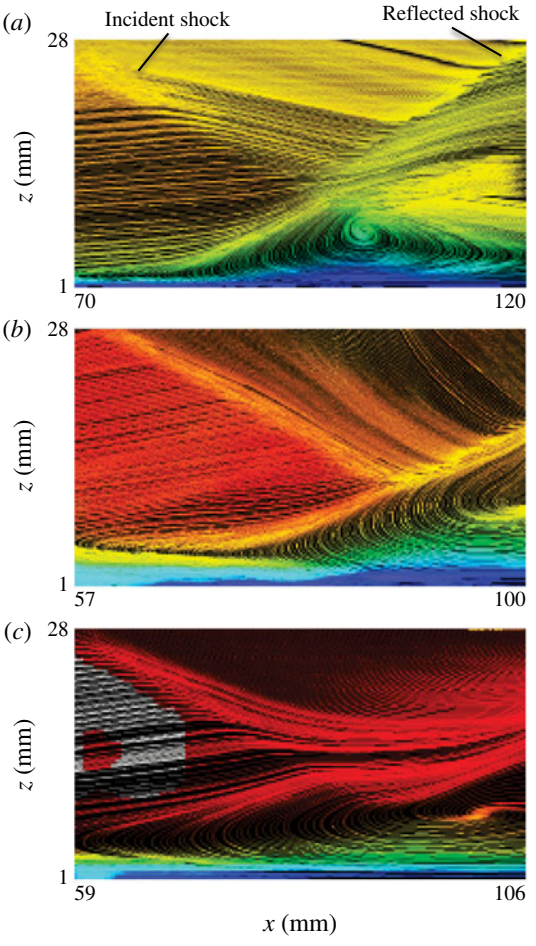


FIGURE 9. (Colour online) Side view of the bottom wall region, visualized using measured Galilean decomposition streamlines. (*a*) Streamwise vertical plane SV1 (on tunnel centreline at $y = 28.5$ mm from sidewall). (*b*) Plane SV2 at $y = 21$ mm, and (*c*) plane SV3 at $y = 17$ mm. Bottom of each image is 1 mm above the bottom wall.

can be concluded that Galilean decomposition streamlines are a useful measure of the existence and location of critical points, but they are not an accurate measure of the sizes of the interaction regions. Instead, the sizes of the interaction regions were determined directly from the PIV data without using (3.1).

3.2. *Centreline region: evidence of Type 2 separation*

Figure 10(*b*) is a top view of Galilean decomposition streamlines in horizontal plane SH1, which is the plane closest to the bottom wall ($z = 9.5$ mm). Streamlines in figure 10 are the projection of the 3-D streamlines onto the x–z plane after the convection velocities (U_{AVG}, W_{AVG}) are subtracted using (3.1).

Figure 10 provides evidence that a Type 2 separation (sketched in figure 10*a*) occurs on the bottom wall near the tunnel centreline. As described in § 1.4, Type 2 separation has three properties: (i) an upstream node (N) that is followed by two saddle

https://doi.org/10.1017/jfm.2014.382 Published online by Cambridge University Press

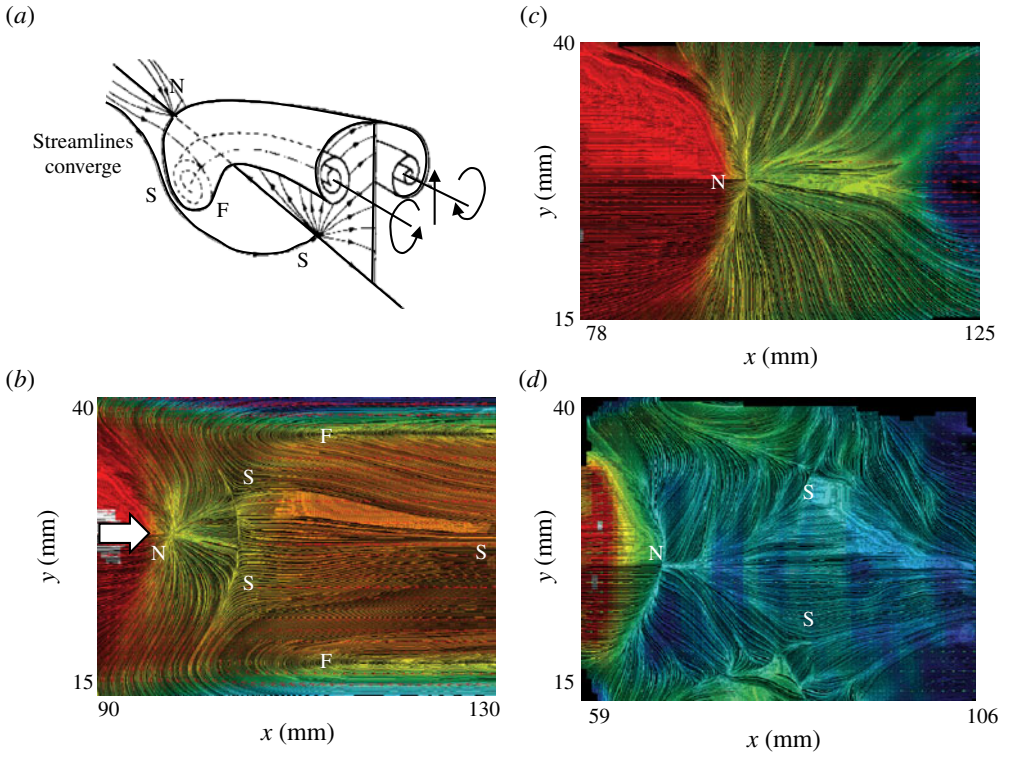


FIGURE 10. (Colour online) Top view of the bottom wall region, showing evidence of a Type 2 separation, as sketched in (*a*). (*b*) Plane SH1 (closest to bottom wall, $z = 9.5$ mm) showing upstream streamlines converging into node N. (*c*) Plane SH2 at $z = 19$ mm and (*d*) plane SH3 at $z = 28.5$ mm.

points (S); (ii) streamlines that converge as they enter the node from upstream; and (iii) a horseshoe vortex that rotates as to create an upflow, as sketched in figure 10(*a*).

In figure 10(*b*) the measured streamlines converge toward a node. Two downstream saddle points occur where the streamlines have a hyperbolic shape. Two focus points are the points about which the streamlines swirl. In figure 10(*c*) the foot of the incident shock wave is the right-hand boundary of the parabolic-shaped (undisturbed) free-stream region. The shock is seen to be highly curved and concave to the incoming flow. Planes SH1, SH2 and SH3 are located at 9.5, 19 and 28.5 mm from the bottom wall, respectively.

Note that there are six critical points in figure 10(*b*) and that they have some features that are similar to the 'owl-face' pattern that was drawn in figure 4(*a*). In figure 10(*b*) our SBLI is seen to create an upstream node followed by two saddle points, two focus points and a saddle point. The owl-face pattern in figure 4(*a*) also has six critical points, however, they are arranged differently. An upstream saddle point is followed by two focus points, two saddle points and then a node. The six SBLI critical points are in the opposite order, i.e. they are identical to the owl-face pattern if the direction of the flow was reversed.

Since a horseshoe vortex is one component of the separation sketched in figure 10(*a*), we looked for evidence of counter-rotating pairs in the vorticity measurements. Figure 11(*a*) is a plot of contours of the streamwise vorticity (ω_x)

https://doi.org/10.1017/jfm.2014.382 Published online by Cambridge University Press

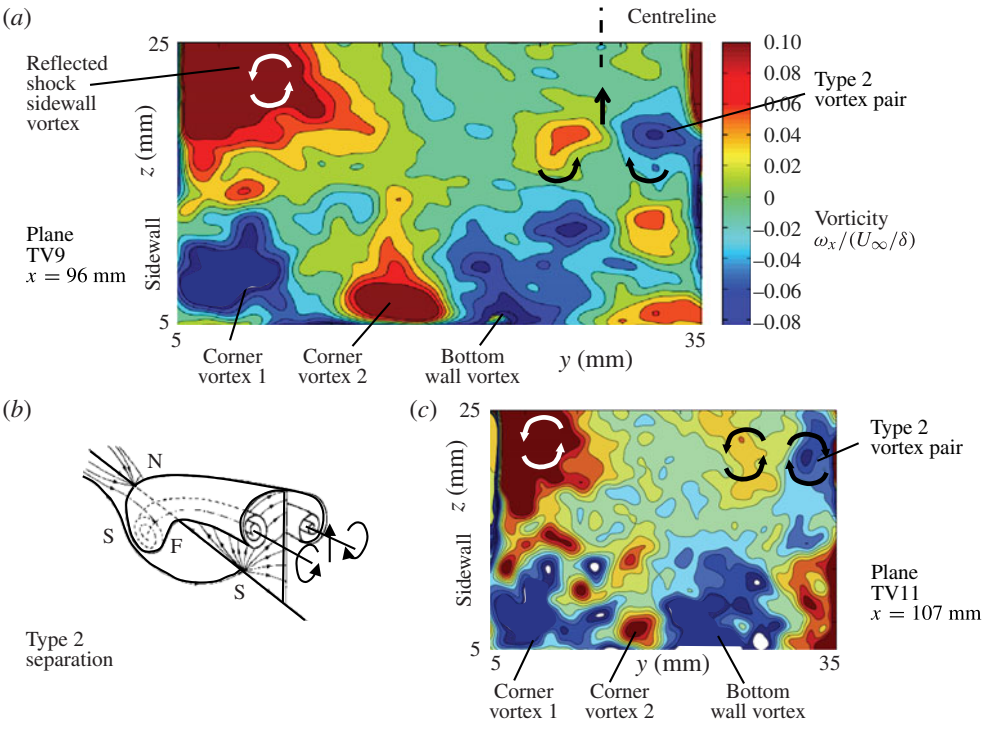


FIGURE 11. View looking upstream of vorticity contours (ω_x) in (*a*) transverse vertical plane TV9 at $x = 96$ mm and (*c*) plane TV11 at $x = 107$ mm. Both (*a*) and (*c*) provide evidence of the horseshoe vortex that was sketched in (*b*) by Tobak & Peake (1982). Vortices rotate so as to create upflow (and inflow) near the centreline. Also seen are sidewall and corner vortices. Here $U_\infty = 594$ m s^{-1} and $\delta = 10.0$ mm.

in the transverse vertical plane near the centre of the shock reflection (plane TV9, $x = 96$ mm). A vortex pair exists 18 mm above the bottom wall and near the centreline. This vortex pair is similar to the vortex pair in the Type 2 separation pattern. The x direction is out of the paper and the left half of the vortex pair has a positive value of ω_x, so the right-hand rule states that the flow around it should be counterclockwise, as is drawn. The flow about the vortex on the right side must be clockwise, as drawn. This produces an inflow toward the centreline underneath the vortices and an upflow between them. Figure 11(*c*) shows the centreline vortex pair at a farther downstream location (at $x = 107$ mm, plane TV11).

Figure 11 shows that the vorticity region associated with sidewall separation is large and it has a large value of $\omega_x/(U_\infty/\delta)$ equal to 0.1, where U_∞ is 594 m s^{-1} and the boundary layer thickness (δ) is 10.0 mm at the upstream location $x = -75.5$ mm. In contrast, the counter-rotating vortices identified with the black arrows near the centreline are small and contain a vorticity value that is less than half of the sidewall region.

The large region of positive vorticity (red) in the upper left of figure 11(*a*) is the sidewall separation vortex that is created by the adverse pressure gradient imposed by the reflected shock wave near the sidewall. The centre of the sidewall vortex is inclined to be parallel to the shock wave and it remains approximately 6 mm from the sidewall. Near the corner there is seen a large negative vorticity region and to

https://doi.org/10.1017/jfm.2014.382 Published online by Cambridge University Press

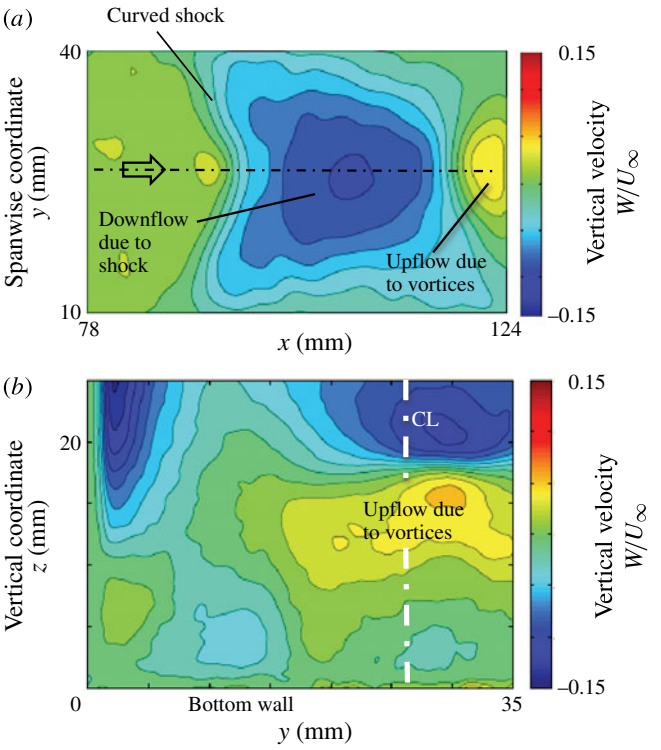


FIGURE 12. (*a*) Top view of velocity contours (W) in plane SH2 showing upflow caused by the horseshoe vortex sketched in figure 11(*b*). (*b*) Upstream view of vertical velocity contours W in plane TV8 ($x = 96$ mm) providing a different view of the upflow.

the right of it exists a large positive vorticity region. The centres of these two corner vortices lie along the bottom wall and run downstream. Figure 11(*a*) shows that the (blue) negative vorticity region remains near the corner, while the (red) positive vorticity region has moved halfway to the centreline. This creates a large zone of flow disturbance in the corner which directs a lateral flow inward toward the centreline and leads to the Type 2 separation shown in figure 11(*b*).

Additional evidence of Type 2 separation is the upward velocity region above the centreline that is marked in figure 12(*a*,*b*). The horseshoe vortex rotates in a way such as to induce upflow near the centreline, as seen in the top and upstream views (figure 12*a*,*b*). This upflow previously was seen in the side view (figure 7*b*).

3.3. *Sidewall region: evidence of Type 1 separation*

Shock wave curvature arises because the flow first separates in the bottom corners at an x-location upstream of the centreline interaction. This can be explained by the fact that the corner contains a large region of low-speed flow where the boundary layers from two walls (sidewall and bottom wall) merge. Thus, the adverse pressure gradient imposed by the shock wave reflection can spread over a large upstream distance. In contrast to the corner region, the separation region on the centreline does not spread as far upstream because only one wall is imposing forces that reduce the flow velocity.

Figure 13(*a*) provides evidence that there is a focus point on the sidewall. After the tunnel was started, oil streak lines were observed to wind up into a tight spiral

https://doi.org/10.1017/jfm.2014.382 Published online by Cambridge University Press

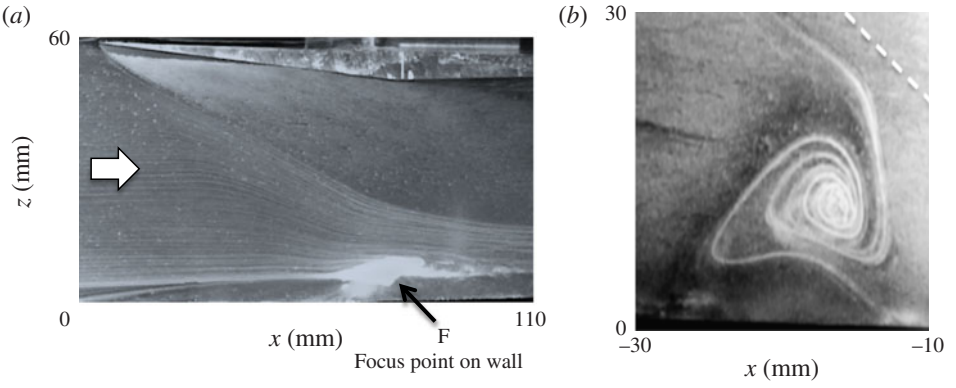


FIGURE 13. (*a*) Sketch of a focus point on a wall for a Type 1 separation (Tobak & Peake 1982); (*b*) focus point on tunnel sidewall identified by oil lines for our 6° wedge; (*c*) larger focus point observed when the 6° wedge is temporarily replaced by a 10° wedge.

pattern on both tunnel sidewalls. The resulting focus point from one sidewall is shown in figure 13(*b*) as a white oval that is centred at $x = 83$ mm and $z = 10.3$ mm. The oil streak lines near this focus point rapidly overlap, so to better visualize the lines, the standard 6° wedge that was used for all aspects of this study was temporarily replaced with a 10° wedge only to record figure 13(*c*). The stronger shock wave creates a larger focus point in which spiral-shaped limiting streamlines can be photographed. Burton & Babinsky (2012) also photographed a large focus point on their sidewall caused by a Mach 1.5 normal shock wave.

The vorticity region that is labelled as the bottom wall vortex in figure 11(*a*,*c*) is believed to be similar to one of the vortex structures that extend downstream in the owl-face pattern of figure 4(*b*). We note that both our SBLI flow pattern (figure 10*b*) and the owl-face pattern have six critical points. Our SBLI streamline forms an upstream node followed by two saddle points, two focus points and a saddle point. Owing to these similarities it is possible that the vortex that extends downstream in the owl-face pattern is analogous to the bottom wall vortex in figure 11(*a*).

Figure 14 demonstrates how the contours of streamwise velocity, U, evolve through the interaction. No sidewall disturbance is observed at $x = 0$ (the wedge leading edge), while a disturbance is observed at $x = 76$ mm. The disturbed region becomes largest at $x = 91$ mm, where it extends approximately 45 % of the distance from the sidewall to the centreline. This x-location is near the centre of the shock reflection on the centreline. Downstream the size of the sidewall interaction region is seen to decrease.

The size of the sidewall interaction region is also seen in figure 15. This is a top view of the profiles of the lateral velocity (V). The tunnel centreline is marked with a straight dashed line and the sidewall ($y = 0$) is just below the horizontal axis. The contour $V = 40$ m s^{-1} is a curved dashed line that is one possible indicator of the sidewall interaction region. This dashed line is extrapolated upstream to indicate that the location of upstream influence begins at approximately $x = 68$ mm on the sidewall. This is far upstream of the centre of shock reflection on the centreline, which occurs at $x = 96$ mm.

In figure 16 we provide additional evidence of lateral inflow toward the centreline that originates in the corner. Contours of lateral velocity V are plotted in 16(*a*) and indicate substantial lateral velocity occurs upstream of the bottom wall centre of

https://doi.org/10.1017/jfm.2014.382 Published online by Cambridge University Press

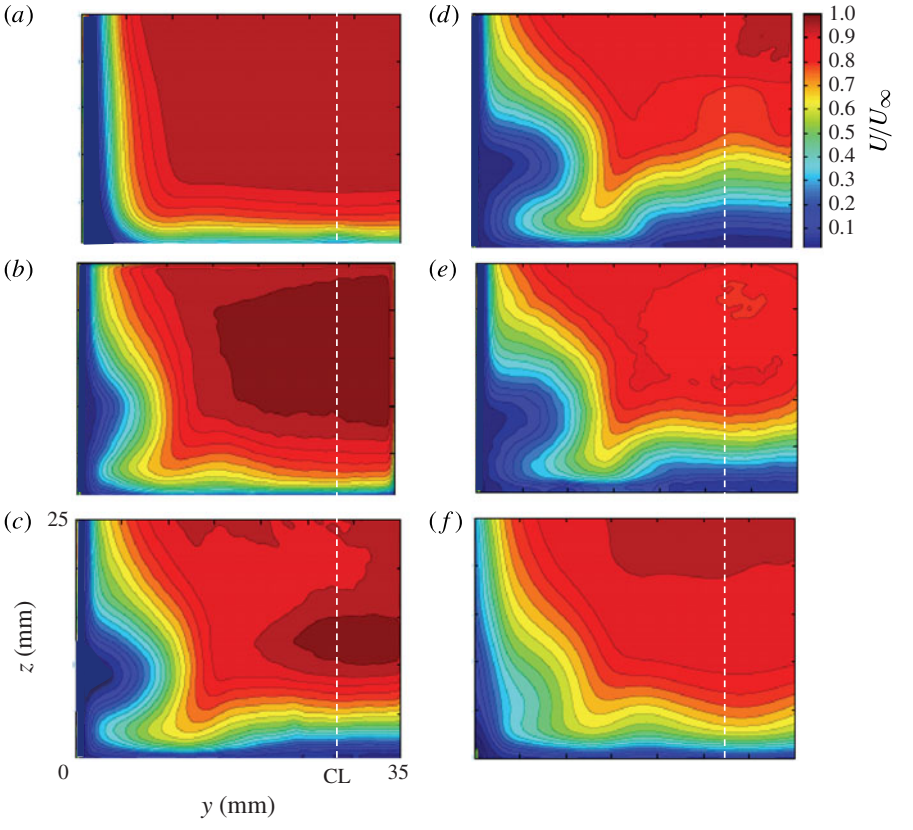


FIGURE 14. Upstream view of the sidewall region: (*a*) $x = 0$ mm; (*b*) $x = 76$ mm; (*c*) $x = 81$ mm; (*d*) $x = 91$ mm; (*e*) $x = 107$ mm; (*f*) $x = 160$ mm. Contours of mean velocity U. The dotted line is the tunnel centreline; the left side of images is within 1 mm of the sidewall.

shock reflection ($x = 96$ mm). The oil streak lines on the bottom wall are presented in figure 16(*b*); they form an hourglass pattern of limiting streamlines. They show that the limiting streamlines rapidly diverge away from the corner, which is consistent with the Type 1 separation sketched in figure 3(*a*). The hourglass shape is consistent with the inflow velocity contours in figure 16(*a*). Hourglass oil lines previously were measured by Bruce *et al.* (2011) for a Mach 1.5 normal shock wave in a duct. Figure 16(*c*) presents a side view of the lateral velocity contours; it indicates where the lateral inflow is largest in plane SV2.

Another view of the sidewall interaction region is presented in figure 17. Galilean decomposition streamlines are plotted in the transverse vertical plane TV9 at $x = 96$ mm. The view is looking upstream. Streamlines spiral about the sidewall vortex (V) while at two locations (S) near the walls the streamlines are hyperbolic-shaped, which indicates where saddle points exist. The streamlines converge near the shock wave, as they did in figure 9.

4. Discussion

Our best estimate of the overall flow pattern that is consistent with the velocity data set is sketched in figure 18(*a*). Below this sketch are measured vorticity contours.

https://doi.org/10.1017/jfm.2014.382 Published online by Cambridge University Press

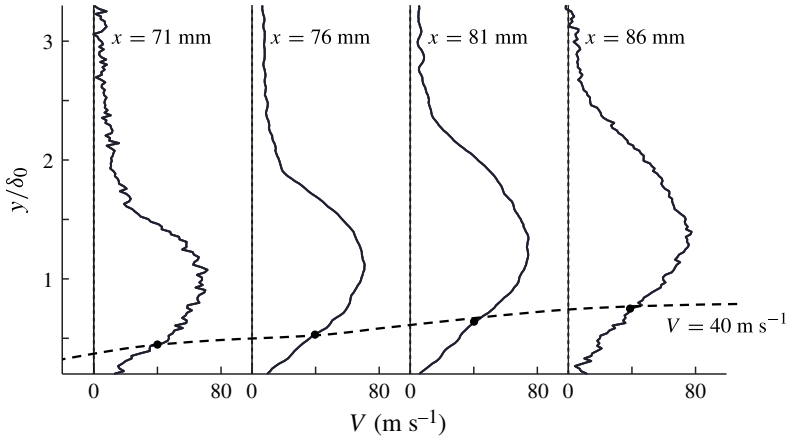


FIGURE 15. (Colour online) Top view of the sidewall region, showing profiles of lateral velocity V versus lateral distance (y). Height (z) is 10.0 mm. The dotted line is $V =$ 40 m s^{-1}. Here $\delta = 10$ mm.

The underlying mechanism consists of several vortex structures. Note that each of the structures drawn in the outflow plane in figure 18(*a*) also is seen in the vorticity data in figure 18(*b*). Corner vortex 1 was found to remain in the corner in all of the transverse data planes. However, corner vortex 2 is seen to be forced away from the sidewall and has moved halfway to the tunnel centreline. This is consistent with the hourglass-shaped oil lines in figure 16(*b*) that are one indicator of the lateral flow pattern.

The sidewall separation induces lateral velocities that force streamlines on the bottom wall to converge into a separation node on the centreline (that is labelled in figure 18*a*). At the node the fluid rapidly rises from the bottom wall. It is argued that the pattern near the node has some similarities to the Type 2 separation sketched in figure 3(*b*), but it has some differences as well. Similarities include: a leading edge node followed by two saddle points, converging streamlines upstream and a vortex pair downstream (all seen in figures 10 and 18*b*). The one difference is that there also exists a bottom wall vortex that is labelled in figure 18(*a*). It runs in the transverse direction underneath the centre of the shock wave reflection then it is deflected downstream and appears in the vorticity data in figure 18(*b*). It causes the upflow and downflow near the bottom wall that are marked in figure 7.

Another vortex tube appears as the large red vorticity region on the upper left side of figure 18(*b*). It is labelled the 'reflected shock vortex'. This vortex is inclined at an angle as it runs along the sidewall underneath where reflected shock bifurcates, as was drawn in figure 1. In transverse data planes (not shown) that are farther upstream of plane TV9 a similar large red region of vorticity is recorded, but it is due to the incident shock and not the reflected shock.

The complex flow pattern in figure 18(*a*,*b*) is due to fact that sidewalls, corners and shock waves alter the way that vorticity is distributed in space. Consider an infinitely wide wind tunnel with no wedge to create a shock wave. All the vorticity would be confined to the upper and lower wall boundary layers. Adding sidewalls and corners creates corner vortices that represent the redistribution of the vorticity that was created at the walls by the no-slip condition. Similarly, adding the wedge and the resulting

https://doi.org/10.1017/jfm.2014.382 Published online by Cambridge University Press

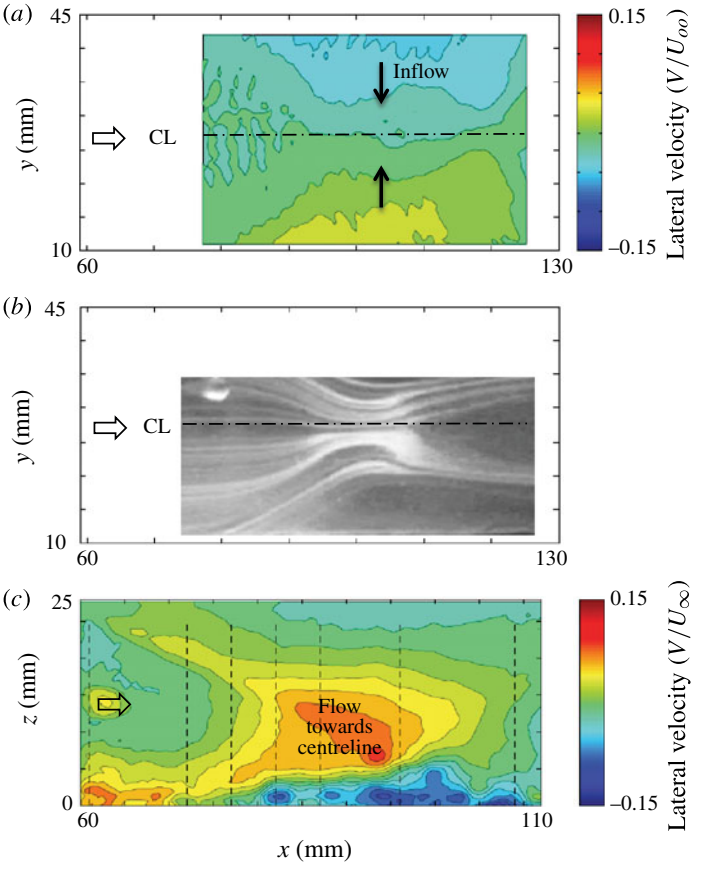


FIGURE 16. (*a*) Top view of lateral inward velocities directed toward the centreline caused by sidewall flow separation (plane SH2). (*b*) Oil streak lines on the bottom wall. (*c*) Side view of the lateral velocity contours in plane SV2.

oblique shock wave causes a further redistribution of the vorticity that was created at the walls. Not only does the shock wave redistribute the vorticity, the vorticity then alters the shock wave. The concentrated vorticity in the vortex tubes alters the flow pattern, and Burton *et al.* (2011) explain that the altered flow pattern then changes the way the adverse pressure gradient is distributed in space. Two-way interactions exist between the curved shock wave and the imposed pressure gradient as well as between the vortex tube magnitudes and trajectory and the general flow arrangement. Following this logic, it is possible that the growth of the sidewall separation zone, and its redistribution of corner vorticity via lateral inflow, may reduce the size of the bottom wall separation zone. That is, increasing sidewall separation makes the duct narrower which reduces the core flow area.

5. Conclusions

(*a*) The interactions between two separation regions (on the sidewall and bottom wall) were measured for the case of a SBLI within a rectangular duct. The roles of the lateral velocities and the vorticity field were quantified. Until now no

https://doi.org/10.1017/jfm.2014.382 Published online by Cambridge University Press

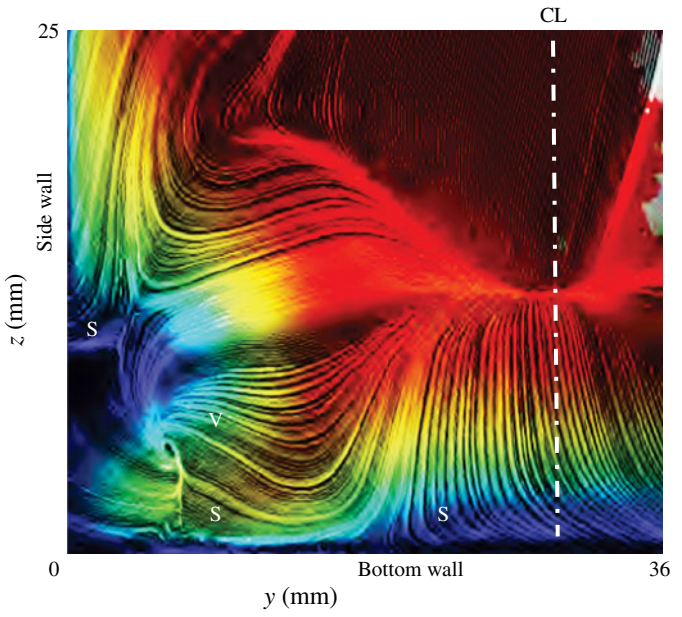


FIGURE 17. (Colour online) Hyperbolic-shaped streamlines (S) and vortex (V) in transverse vertical plane TV9. Flow is out of the paper. Galilean decomposition streamlines are plotted at $x = 96$ mm, which is near the centre of the shock reflection off the bottom wall.

complete data base has been available that includes lateral velocity and vorticity. Three components of the velocity were measured using stereo-PIV on 25 data planes aligned in all three orthogonal directions.

(*b*) In this study over 45 % of the bottom wall experienced significant lateral velocities caused by the sidewalls. For flows in low-aspect-ratio ducts, managing the sidewall separation is a priority. Results cannot be explained by the conventional concept of a 2-D separation bubble, since lateral velocities are so large that the flow is everywhere 3-D.

(*c*) The underlying 3-D flow field is sketched in figure 18; it was identified using the measured vorticity field, the lateral velocity data, the oil flow patterns and the Galilean decomposition streamlines. Five separate vortex structures are labelled: (i) corner vortex 1, (ii) corner vortex 2, (iii) bottom wall vortex, (iv) incident shock sidewall vortex and (v) reflected shock sidewall vortex.

(*d*) Separation begins upstream in the corners because two walls exert retarding forces; the flow is similar to the Type 1 pattern drawn in figure 3(*a*). Sidewall separation forces lateral flow to converge toward a node on the centreline and leads to streamlines that have similarities to the Type 2 pattern that is drawn in figure 3(*b*). Fluid must lift off the bottom wall at the node and this creates a Type 2 vortex pair seen in figure 18. A bottom wall vortex lies underneath the shock reflection. Other vortices lie along the sidewalls where the incident and reflected shocks intersect the sidewalls. Measurements verify the existence of the node and saddle points (figure 10), vortex structures (figures 7, 11 and 18) and a sidewall focus point (figure 13).

https://doi.org/10.1017/jfm.2014.382 Published online by Cambridge University Press

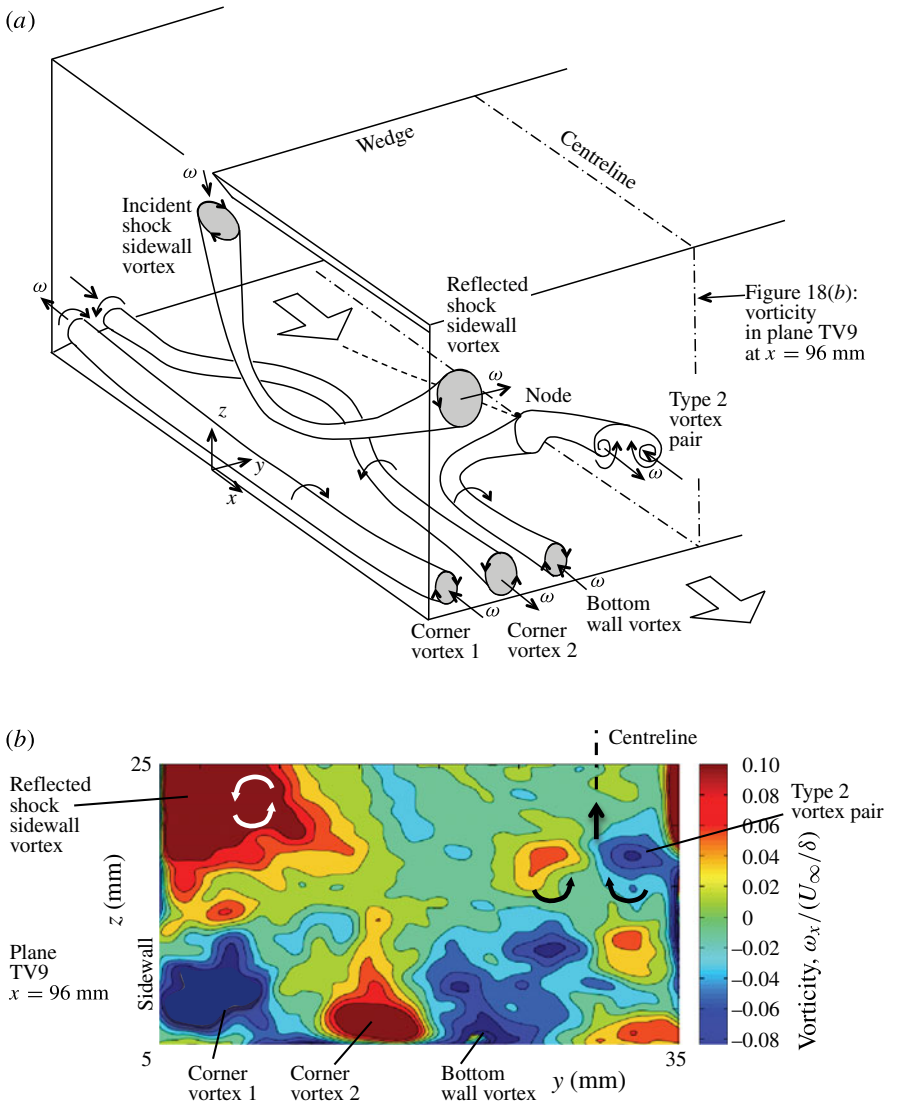


FIGURE 18. Schematic of the overall flow pattern that was determined for a SBLI in a rectangular duct. The shock wave structure is not drawn; it appears in figure 1.

(*e*) Vorticity field images indicate that sidewall vorticity $\omega_x/(U_\infty/\delta)$ has the relatively large value of 0.1. This is more than twice the value of vorticity measured in the bottom wall separation region.

(*f*) Results are consistent with the general ideas of Burton & Babinsky (2012) who have explained how the sidewalls and corners create compression waves that redistribute the adverse pressure gradient in space. The present lateral velocity and vorticity measurements show how the flow structure adjusts to accommodate this redistribution of the pressure gradient.

https://doi.org/10.1017/jfm.2014.382 Published online by Cambridge University Press

Acknowledgements

The work was one activity of the US Air Force Collaborative Center for Aeronautical Sciences that was supported by the Air Force Research Laboratory, Air Vehicle Directorate, AFRL/RB. The project was monitored by Dr J. Benek and Dr J. Tinapple. The authors are grateful for discussions with Professor M. Gamba and for assistance provided by R. Morajkar and R. Klomparens in analysing some of the data.

Appendix A. Uncertainties in the measurements

Uncertainty in the velocity data was assessed in several ways. PIV data indicated that the free-stream value of U_∞ was 594 m s^{-1}, which was within 2 % of the value determined from the measured stagnation and wall pressures. Previous measurements of Lapsa & Dahm (2011) showed that particle lag error exceeded 3 % in the region that is 1.9 mm downstream of our oblique shock wave but is less than 3 % at other locations. They compared their measured velocities downstream of the shock (on tunnel centreline) with values given by the inviscid shock tables and they used the same oil drops and PIV system as described above. Velocity values also were checked along lines where perpendicular PIV data planes intersect. In some cases the velocity in one plane appeared to be shifted in the x direction by approximately 2 mm from the data in the other plane, indicating that the x-location of one plane was measured incorrectly. The problem was corrected by re-acquiring data in 4 of the 25 data planes and more carefully measuring their x-locations. Data where the two planes intersect then agreed to within 3 %. Boundary layer profiles to within 0.5 mm of the wall were repeatable to within 2 % (Lapsa & Dahm 2011).

The quality of the flow in the supersonic tunnel, with the wedge removed, was assessed from wall static pressure measurements. Wall pressures deviated by less than 3 % from the isentropic value within the upstream 70 % of the test section (from $x = -85$ mm to $x = 25$ mm). In the downstream 30 % of the test section, static pressure rose slowly in the x direction to 19 % above the isentropic value. Most of this gradual pressure rise can be explained by the expected growth of the boundary layer displacement thickness along the tunnel sidewalls, which are parallel. The displacement thickness was measured to be 1.47 mm at $x = -75.5$ mm by Lapsa & Dahm (2011). It is expected to grow to 2.56 mm at the end of the test section, based on a standard $x^{4/5}$ scaling so the core area is expected to be reduced by 7.0 %. The isentropic relations indicate that such an area decrease causes the static pressure to rise by 13 %. The remaining 6 % of measured pressure rise is not explained and may be due to imperfections in the nozzle or tunnel sidewall. Schlieren images detected one weak wave emanating from a bottom wall insert plate but this wave has a wave angle only 1° larger than the Mach angle, so it can contribute no more than a 3 % pressure rise. No other waves were observed.

Statistical uncertainty arises due to the number (N) of PIV images that are used to determine the mean values. Here N was selected to be 1700 images. Statistical analysis predicts that the 98 % confidence interval in gas velocity (CI_{98}) is given by

$$\frac{CI_{98}}{U_e} = \pm 2.33 \frac{\sigma_u / U_e}{\sqrt{N}}. \tag{A 1}$$

This means that if 100 ensembles of data are collected and each ensemble contains $N = 1700$ PIV images, 98 of these ensembles should have a mean velocity that differs from the expectation value (U_e) by less than 2.33 $\sigma_u/\sqrt{N}$. The expectation value U_e is

https://doi.org/10.1017/jfm.2014.382 Published online by Cambridge University Press

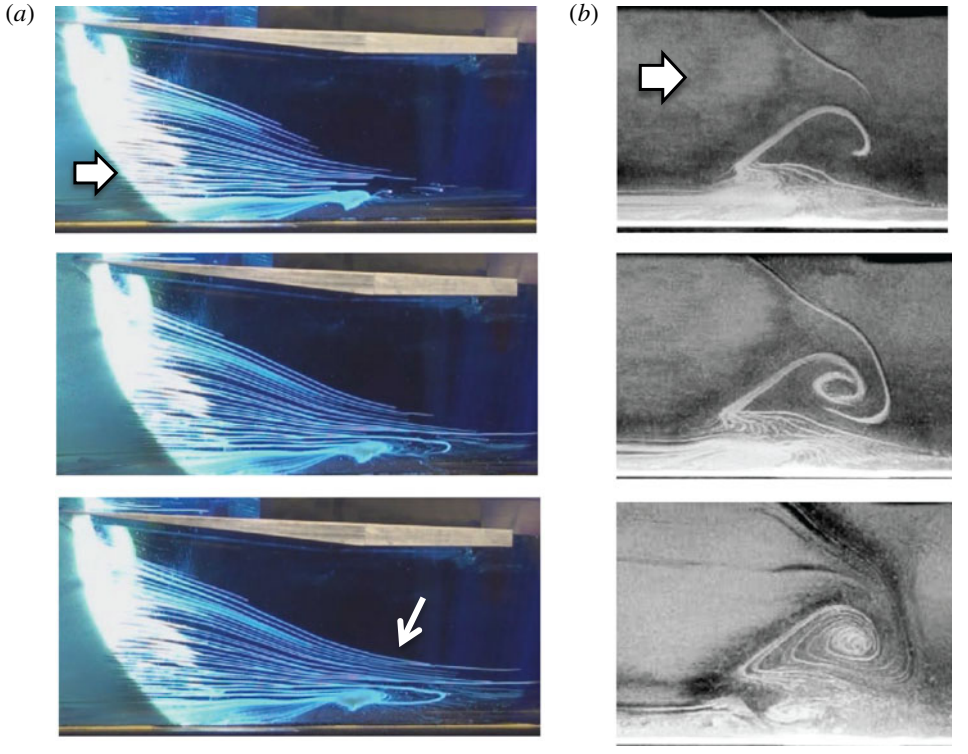


FIGURE 19. (Colour online) Photographs of oil lines on the sidewall from movies taken during tunnel startup for (*a*) the normal six-degree wedge and (*b*) the ten-degree wedge that is temporarily inserted to better visualize oil lines.

the mean that would be computed if an ensemble contained an infinite number of PIV images. The normalized standard deviation $\sigma_u/\sqrt{N}$ was measured to be 0.02 in the free stream and was less than 0.06 in the boundary layer and flow separation regions of interest. Inserting these value into the equation indicates that the confidence interval divided by U_e is 0.1 % in the free stream and 0.3 % in the boundary layer. Therefore, there is almost no advantage gained by averaging over more than 1700 images.

Appendix B. Time history of oil pattern on sidewall

An interesting oil line pattern appears on the sidewall during the tunnel startup process; it eventually forms the focus point that is seen in figure 13. Figure 19(*a*) contains photographs of the oil lines extracted from movies obtained using the normal six degree wedge that was used for all data collection. As the tunnel is started the oil lines move to the right and are deflected downward by the downward flow behind the incident shock wave. Less than one second later some oil lines near the bottom wall undergo a complete rotation of more than 360° as they roll up into the sidewall focus point that is marked by the arrow. At this time the tunnel has reached the steady-state condition. To better visualize the rollup, a ten-degree wedge was temporarily used to generate figure 19(*b*). Oil lines that are above and below the focus point are seen to roll up during the tunnel startup. Fluid just adjacent to the sidewall should follow

https://doi.org/10.1017/jfm.2014.382 Published online by Cambridge University Press

these oil lines but to conserve mass the fluid also must rapidly move perpendicular to the sidewall near the centre of the focus point.

REFERENCES

ADAMSON, T. C. & MESSITER, A. F. 1980 Analysis of two-dimensional interactions between shock waves and boundary layers. *Annu. Rev. Fluid Mech.* **12** (1), 103–138.

ADRIAN, R. J., CHRISTENSEN, K. T. & LIU, Z.-C. 2000 Analysis and interpretation of instantaneous turbulent velocity fields. *Exp. Fluids* **29** (3), 275–290.

ADRIAN, R. J. & WESTERWEEL, J. 2010 *Particle Image Velocimetry*. Cambridge University Press.

AKILLI, H. & ROCKWELL, D. 2002 Vortex formation from a cylinder in shallow water. *Phys. Fluids* **14** (9), 2957–2967.

ALVI, F. S. & SETTLES, G. S. 1992 Physical model of the swept shock wave/boundary-layer interaction flowfield. *AIAA J.* **30** (9), 2252–2258.

BABINSKY, H. & HARVEY, J. K. 2011 *Shock Wave–Boundary-Layer Interactions*. Cambridge University Press.

BRUCE, P. J. K., BURTON, D. M. F., TITCHENER, N. A. & BABINSKY, H. 2011 Corner effect and separation in transonic channel flows. *J. Fluid Mech.* **679**, 247–262.

BURTON, D. M. F. & BABINSKY, H. 2012 Corner separation effects for normal shock wave/turbulent boundary layer interactions in rectangular channels. *J. Fluid Mech.* **707**, 287–306.

BURTON, D. M. F., BABINSKY, H. & BRUCE, P. J. K. 2011 Experimental investigation of the flow structure for shock wave/boundary layer interactions at an intersecting normal and spanwise plane. In *49th AIAA Aerospace Sciences Meeting, AIAA Paper* 2011-0856. Orlando, Florida: American Institute of Aeronautics and Astronautics.

CANTWELL, B. J. 1981 Organized motion in turbulent flow. *Annu. Rev. Fluid Mech.* **13** (1), 457–515.

CHONG, M. S., PERRY, A. E. & CANTWELL, B. J. 1990 A general classification of three-dimensional flow fields. *Phys. Fluids* A **2** (5), 765–777.

CLEMENS, N. T. & MUNGAL, M. G. 1991 A planar Mie scattering technique for visualizing supersonic mixing flows. *Exp. Fluids* **11**, 175–185.

DEBONIS, J. R., OBERKAMPF, W. L., WOLF, R. T., ORKWIS, P. D., TURNER, M. G., BABINSKY, H. & BENEK, J. A. 2012 Assessment of computational fluid dynamics and experimental data for shock boundary-layer interactions. *AIAA J.* **50** (4), 891–903.

DÉLERY, J. M. 2001 Robert Legendre and Henri Werlé: toward the elucidation of three-dimensional separation. *Annu. Rev. Fluid Mech.* **33** (1), 129–154.

DÉLERY, J. M. 2013 *Three-dimensional Separated Flows Topology*. Wiley-ISTE.

DÉLERY, J. M. & DUSSAUGE, J.-P. 2009 Some physical aspects of shock wave/boundary layer interactions. *Shock Waves* **19** (6), 453–468.

DOERFFER, P. & DALLMANN, U. 1989 Reynolds number effect on separation structures at normal shock wave/turbulent boundary-layer interaction. *AIAA J.* **27** (9), 1206–1212.

DUPONT, P., HADDAD, C., ARDISSONE, J. P. & DEBIÉVE, J.-F. 2005 Space and time organisation of a shock wave/turbulent boundary layer interaction. *Aerosp. Sci. Technol.* **9** (7), 561–572.

DUPONT, P., PIPONNIAU, S., SIDORENKO, A. & DEBIÈVE, J.-F. 2008 Investigation by particle image velocimetry measurements of oblique shock reflection with separation. *AIAA J.* **46** (6), 1365–1370.

EAGLE, W. E. 2012 An experimental study of three-dimensional inlet shock-boundary layer interactions. PhD thesis, University of Michigan at Ann Arbor.

EAGLE, W. E., DRISCOLL, J. F. & BENEK, J. A. 2012 3-D inlet shock-boundary layer interactions – PIV database for the second SBLI workshop. In *30th AIAA Applied Aerodynamics Conference, AIAA Paper* 2012-3214. New Orleans, Louisiana: American Institute of Aeronautics and Astronautics.

GANAPATHISUBRAMANI, B., CLEMENS, N. T. & DOLLING, D. S. 2007 Effects of upstream boundary layer on the unsteadiness of shock-induced separation. *J. Fluid Mech.* **585**, 369–394.

HELMER, D. B., CAMPO, L. M. & EATON, J. K. 2012 Three-dimensional features of a Mach 2.1 shock/boundary layer interaction. *Exp. Fluids* **53** (5), 1347–1368.

HILL, P. & PETERSON, C. 1992 *Mechanics and Thermodynamics of Propulsion*, 2nd edn. Prentice Hall.

https://doi.org/10.1017/jfm.2014.382 Published online by Cambridge University Press

HUMBLE, R. A., ELSINGA, G. E., SCARANO, F. & VAN OUDHEUSDEN, B. W. 2009 Three-dimensional instantaneous structure of a shock wave/turbulent boundary layer interaction. *J. Fluid Mech.* **622**, 33–62.

HUMBLE, R. A., SCARANO, F. & VAN OUDHEUSDEN, B. W. 2007 Particle image velocimetry measurements of a shock wave/turbulent boundary layer interaction. *Exp. Fluids* **43** (2–3), 173–183.

KANDASAMY, M., XING, T. & STERN, F. 2009 Unsteady free surface wave-induced separation: vortical structures and instabilities. *J. Fluids Struct.* **25** (2), 343–363.

KUBOTA, H. & STOLLERY, J. L. 1982 An experimental study of the interaction between a glancing shock wave and a turbulent boundary layer. *J. Fluid Mech.* **116**, 431–458.

LAPSA, A. P. 2009 Experimental study of passive ramps for control of shock-boundary layer interactions. PhD thesis, University of Michigan at Ann Arbor.

LAPSA, A. P. & DAHM, W. J. A. 2011 Stereo particle image velocimetry of nonequilibrium turbulence relaxation in a supersonic boundary layer. *Exp. Fluids* **50** (1), 89–108.

VAN OUDHEUSDEN, B. W., NEBBELING, C. & BANNINK, W. J. 1996 Topological interpretation of the surface flow visualization of conical viscous/inviscid interactions. *J. Fluid Mech.* **316**, 115–137.

PALAU-SALVADOR, G., STOESSER, T., FRÖHLICH, J., KAPPLER, M. & RODI, W. 2010 Large eddy simulations and experiments of flow around finite-height cylinders. *Flow Turbul. Combust.* **84** (2), 239–275.

PANARAS, A. G. 1996 Review of the physics of swept-shock/boundary layer interactions. *Prog. Aerosp. Sci.* **32** (2–3), 173–244.

PERRY, A. E. & CHONG, M. S. 1987 A description of eddying motions and flow patterns using critical-point concepts. *Annu. Rev. Fluid Mech.* **19** (1), 125–155.

PERRY, A. E. & FAIRLIE, B. D. 1974 Critical points in flow patterns. In *Turbulent Diffusion in Environmental Pollution* (ed. F. N. Frenkiel & R. E. Munn), vol. 18B, pp. 299–315. Academic Press.

PRIEBE, S., WU, M. & MARTÍN, M. P. 2009 Direct numerical simulation of a reflected-shock-wave/turbulent-boundary-layer interaction. *AIAA J.* **47** (5), 1173–1185.

SAMIMY, M. & LELE, S. K. 1991 Motion of particles with inertia in a compressible free shear layer. *Phys. Fluids* A **3** (8), 1915–1923.

SOUVEREIN, L. J., DUPONT, P., DEBIÈVE, J.-F., VAN OUDHEUSDEN, B. W. & SCARANO, F. 2010 Effect of interaction strength on unsteadiness in shock-wave-induced separations. *AIAA J.* **48** (7), 1480–1493.

SQUIRE, L. C. 1961 The motion of a thin oil sheet under the steady boundary layer on a body. *J. Fluid Mech.* **11** (02), 161–179.

SURANA, A., GRUNBERG, O. & HALLER, G. 2006 Exact theory of three-dimensional flow separation. Part 1. Steady separation. *J. Fluid Mech.* **564**, 57–103.

SURANA, A., JACOBS, G. B., GRUNBERG, O. & HALLER, G. 2008 An exact theory of three-dimensional fixed separation in unsteady flows. *Phys. Fluids* **20** (10), 107101.

TOBAK, M. & PEAKE, D. J. 1982 Topology of three-dimensional separated flows. *Annu. Rev. Fluid Mech.* **14** (1), 61–85.

WANG, K. C. 1972 Separation patterns of boundary layer over an inclined body of revolution. *AIAA J.* **10** (8), 1044–1050.

WANG, K. C. 1974 Boundary layer over a blunt body at high incidence with an open-type of separation. *Proc. R. Soc. A: Math. Phys. Engng Sci.* **340** (1620), 33–55.

WU, J. Z., TRAMEL, R. W., ZHU, F. L. & YIN, X. Y. 2000 A vorticity dynamics theory of three-dimensional flow separation. *Phys. Fluids* **12** (8), 1932–1954.

https://doi.org/10.1017/jfm.2014.382 Published online by Cambridge University Press